The Curious Case of the "Heartworm" Nebula

W. D. Cotton[1,2] [ID], F. Camilo[2] [ID], W. Becker[3,4], J. J. Condon[1] [ID], J. Forbrich[5] [ID], I. Heywood[2,6,7] [ID], B. Hugo[2], S. Legodi[2], T. Mauch[2] [ID], P. Predehl[3], P. Slane[8] [ID], and M. A. Thompson[9] [ID]

[1] National Radio Astronomy Observatory, 520 Edgemont Road, Charlottesville, VA 22903, USA; bcotton@nrao.edu
[2] South African Radio Astronomy Observatory, 2 Fir Street, Observatory 7925, South Africa
[3] Max-Planck-Institut für extraterrestrische Physik, Giessenbachstraße 1, D-85748 Garching, Germany
[4] Max-Planck-Institut für Radioastronomie, Auf dem Hügel 69, D-53121 Bonn, Germany
[5] Centre for Astrophysics Research, University of Hertfordshire, College Lane, Hatfield AL10 9AB, UK
[6] Astrophysics, Department of Physics, University of Oxford, Keble Road, Oxford OX1 3RH, UK
[7] Department of Physics and Electronics, Rhodes University, PO Box 94, Makhanda 6140, South Africa
[8] Center for Astrophysics, Harvard & Smithsonian, 60 Garden Street, Cambridge, MA 02138, USA
[9] School of Physics and Astronomy, University of Leeds, Leeds LS2 9JT, UK

Abstract

The curious Galactic features near G357.2−0.2 were observed with the MeerKAT radio interferometer array in the UHF and L bands (0.56–1.68 GHz). There are two possibly related features: a newly identified faint heart-shaped partial shell (the "heart"), and a series of previously known but now much better imaged narrow, curved features (the "worm") interior to the heart. Polarized emission suggests that much of the emission is nonthermal and is embedded in a dense plasma. The filaments of the worm appear to be magnetic structures powered by embedded knots that are sites of particle acceleration. The morphology of the worm broadly resembles some known pulsar wind nebulae (PWNe) but there is no known pulsar or PWN which could be powering this structure. We also present eROSITA observations of the field; no part of the nebula is detected in X-rays, but the current limits do not preclude the existence of a pulsar/PWN of intermediate spin-down luminosity.

1. Introduction

Broadbent et al. (1989) identified a feature near G357.2−0.2 (G357.1−00.2 in some references) as a candidate supernova remnant (SNR) because its $S_{60\,\mu m}/S_{6\,cm}$ flux-density ratio is lower than that of Galactic H II regions and it is resolved at 6 cm with the Parkes telescope 4′ beam. Gray (1994) added the 1′ resolution 843 MHz Molonglo Observatory Synthesis Telescope image, clearly resolving a sinuous structure for the first time and indicating a nonthermal radio spectrum. There is a diffuse halo surrounding the fine-scale structure.

Gray (1996) was the first to present and discuss high-resolution (13″) Very Large Array images of this nebula. The author also noted the high polarization of the filaments at C band (5 GHz) and the low polarization at L band (1.5 GHz), indicating depolarization and rotation measure RM ∼ 2000 rad m^{-2}. On the basis of the unusual morphology, Gray (1996) deprecated the SNR interpretation and mentioned a variety of possibilities, including a pulsar wind nebula (PWN) and one more example of peculiar nonthermal phenomena near the Galactic center (e.g., the "Tornado" only 0°.5 away from G357.2−0.2; Gaensler et al. 2003).

Gray (1994, 1996) note that the pulsar B1736−31 is in the vicinity of G357.2−0.2, in projection. Its location outside the nebula precludes any connection to a PWN interpretation, and its spin-down age of 0.5 Myr (Clifton et al. 1992) also makes it too old to still have an associated visible SNR.

HI observations of G357.2−0.2 by Roy & Rao (2002) give a distance of at least 6 kpc and place it either in front of, or partly embedded in, a cloud believed to be beyond the Galactic center; they conclude that it is Galactic.

We observed G357.2−0.2 with the MeerKAT radio telescope[10] in the UHF and L bands (0.56–1.68 GHz) with 7″ resolution and with the extended Röntgen Survey Imaging Telescope Array (eROSITA) X-ray instrument. The observations and analysis are described in Section 2, the imaging results are presented in Section 3, and a discussion of these results is in Section 4 followed by a summary in Section 5.

2. Observations and Data Analysis

2.1. MeerKAT Observations, Analysis, and Imaging

We observed G357.2−0.2 in both L (886–1682 MHz) and UHF (563–1068 MHz) bands with the 64 antenna MeerKAT array pointed at J2000 R.A. = 17^{h}39^{m}39^s.82, decl. = −31°27′47″.0 (G357.176−0.235). The integration time was 8 s, and each band was divided into 4096 spectral channels.

The observations were in two sessions, L band on 2020 July 21 for 8 hr with 59 antennas and UHF on 2020 August 18 for 8 hr with 53 antennas. PKS B1934−638 was used as the flux density, bandpass and delay calibrator, 3C 286 as the polarization calibrator, and J1830−3602 as the astrometric calibrator. The observing sequence cycled between J1830−3602 (2 minutes) and G357.2−0.2 (20 minutes) with a flux/bandpass calibrator (10 minutes) every 2 hr. Our flux-density scale is

---
[10] Operated by the South African Radio Astronomy Observatory (SARAO).

based on the Reynolds ([1994](#)) spectrum of PKS B1934−638:

$$\log(S) = -30.7667 + 26.4908(\log \nu) - 7.0977(\log \nu)^2 \\ + 0.605334(\log \nu)^3 \,, \tag{1}$$

where S is the flux density in jansky and ν is the frequency in megahertz.

2.1.1. Analysis

Data flagging and calibration were performed as described for L-band data in Mauch et al. ([2020](#)) and Cotton et al. ([2020](#)). The UHF session was calibrated independently, and we have adopted the L-band procedure for the UHF data with some band-specific modifications described below.

First, we trimmed 144 channels from each edge of the UHF band to account for the roll-off in receiver response, leaving a frequency range 563–1069 MHz. We then used a UHF-specific mask to identify frequency ranges that contain persistent and strong radio-frequency interference (RFI). This covers only 934–960 MHz, where cellular communication signals are present. After combining our empirical mask with the editing steps described in Mauch et al. ([2020](#)) during calibration, ∼10% of the target data were flagged from the trimmed UHF band.

The data were split into eight sub-bands with equal frequency width and these were calibrated independently. We used a UHF sky model extrapolated from the L-band model of the PKS B1934−638 field containing the power-law spectra of sources appearing brighter than 1 mJy beam^{-1} at 1.3 GHz within 1° of PKS B1934−638. The flux density of PKS B1934−638 in each sub-band was obtained from Equation ([1](#)), and used to derive the amplitude spectrum of J1830−3602. The amplitudes of the gains measured from J1830−3602 were scaled by a smooth model fitted to its measured flux densities in each sub-band, and the scaled amplitude and phase corrections were interpolated in time and applied to the target data. The data were reweighted using the root mean square (rms) in the observed visibilities in 10 minute intervals.

The above extrapolation does not account for sources toward the edge of the wider UHF field of view (FOV). However, we have compared the above analysis to one that uses a preliminary model of the full UHF FOV of PKS B1934−638, and find no appreciable difference in the derived flux scales above 700 MHz. Below this frequency our derived flux densities are somewhat (up to 10%–20%) overestimated.

Imaging used the wide-band, wide-field imager MFImage in the Obit package[11] (Cotton [2008](#)) as described in Mauch et al. ([2020](#)) and Cotton et al. ([2020](#)). MFImage (described in detail in Cotton et al. [2018](#)) uses faceting to account for the noncoplanarity of the MeerKAT baselines and multiple frequency bins which are imaged independently and CLEANed jointly to account for frequency variations in the sky and the antenna pattern. Imaging used Robust weighting (−1.5 in AIPS/Obit usage) to down-weight the central condensation of antennas in the array and improve the resolution.

2.1.2. Total-intensity Imaging

The data in the two frequency bands were imaged independently. With the large bandwidth covered by the data,

the shortest baseline length in wavelengths varied by a factor of three between the highest and lowest frequencies in the two bands. Due to the large-scale emission in the field, if uncorrected, this will lead to a variable fraction of the total intensity recovered as a fraction of frequency and a frequency-dependent negative bowl around the extended emission. This will artificially cause the spectrum to appear steeper than it actually is. In order to counteract this, an inverted Gaussian taper centered at the origin was applied to the weights of the shortest baselines with a Gaussian σ of 500 wavelengths to both the UHF and the L-band data. This will suppress emission on scales larger than ∼200″, and is similar to the spectral index analysis in Cotton et al. ([2020](#)). A multiresolution CLEAN was used to help recover the very extended emission in the field.

The L-band total-intensity data were imaged to a radius of 1° plus outlier facets to a distance of 1°.5 to cover sources expected to appear brighter than 1 mJy beam^{-1} based on the SUMSS catalog at 843 MHz (Mauch et al. [2003](#)). Three iterations of phase-only self-calibration were applied. The total bandpass was divided into $14 \times 5\%$ fractional bandwidth bands giving unequal widths in frequency. L-band total-intensity imaging used 366,886 components stopping at a depth of 45 μJy beam^{-1} with a total flux density of 23.7 Jy; the off-source rms noise was 20 μJy beam^{-1}. The CLEAN restoring beam was an elliptical Gaussian with FWHM axes 7″.0 × 6″.8 at position angle 0°.

At UHF an FOV with radius 2°.5 was imaged in $14 \times 5\%$ fractional bands with phase self-calibration using 419,484 components to a minimum of 200 μJy beam^{-1} and a total flux density of 60.9 Jy. Outliers were added up to 3°.5 from the pointing. The off-source rms was 89 μJy beam^{-1}. The CLEAN restoring beam was 11″.6 × 10″.3 at position angle −20°.

For both L band and UHF, the 8 s integrations and sub-bands used introduced negligible time and bandwidth smearing (<2″) across the full imaged FOVs.

2.1.3. Deconvolution of Stokes Q and U

Only the L-band data had adequate polarization calibration and were imaged in Stokes Q and U. In order to recover the polarimetry in the presence of the large Faraday rotation of polarized emission, a relatively high spectral resolution was used for Stokes Q and U imaging—a 1% fractional bandwidth resulting in 68 sub-bands across the band. The deconvolution also used the joint polarization CLEAN described in Condon et al. ([2021](#)). Linear polarization imaging used 50,000 CLEAN components to a depth of 54 μJy beam^{-1} resulting in an off-source rms of 10 μJy beam^{-1}.

2.2. eROSITA Observations and Analysis

The X-ray eROSITA (Predehl et al. [2021](#)) is one of two instruments on the Spectrum Röntgen−Gamma observatory (Sunyaev et al. [2021](#)). It consists of seven aligned X-ray telescopes (TM1–TM7) which have an FOV of 1°. All telescopes observe the same sky region simultaneously in the 0.2–8 keV bandpass. In survey mode, the instrument's angular resolution is 26″. eROSITA started its first all-sky survey on 2019 December 13, with eight such surveys planned over four years (see Predehl et al. [2021](#)).

The X-ray data we report here were taken during the first four eROSITA surveys, eRASS:4. By end 2021 the position of G357.2−0.2 had been observed with a total of 27 telescope
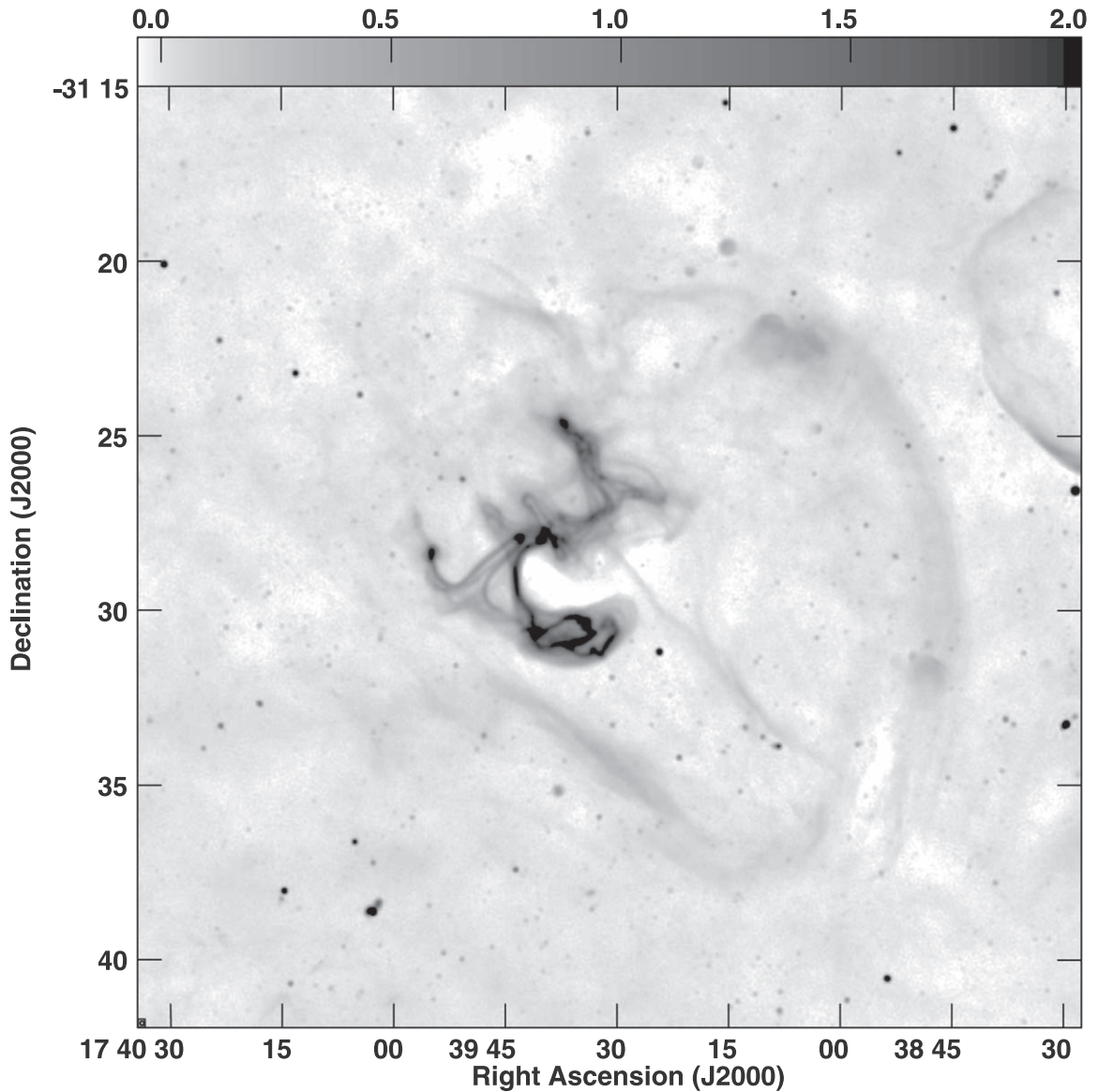
---

[11] http://www.cv.nrao.edu/~bcotton/Obit.html

Figure 1. Reverse gray-scale of the L-band (886–1681 MHz) Stokes I image of G357.2−0.2 (the Heartworm) in double log stretch with a scale-bar at the top labeled in mJy beam^{-1}. The resolution is shown in the box at lower left. This rendering optimizes the display of the larger-scale low-brightness emission, including the shell-like heart-shaped feature spanning $\sim 18'$ northward from (R.A., decl.) $\approx (17^h39^m15^s, -31°38')$. The central fine-scale features, considerably saturated in this view, are best discerned in Figure 2.

passages during four epochs, 2020 March 27–28, 2020 September 28–30, 2021 March 24–25, and 2021 September 24–25, resulting in an unvignetted averaged exposure time of 1048 s.

The data used in our analysis were processed by the eROSITA Standard Analysis Software System (eSASS) pipeline and have the processing number #946. For the data analysis we used eSASS version 201009.[12] Within the eSASS pipeline, X-ray data of the eRASS sky are divided into 4700 partly overlapping sky tiles of $3°6 \times 3°6$ each. These are numbered using six digits, three each for R.A. and decl., encoding the sky tile center position in degrees. The majority of G357.2−0.2 falls into the eRASS tiles 266120 and 266123, with the surrounding tile 263123 also required for a complete coverage of G357.2−0.2.

---

[12] See https://erosita.mpe.mpg.de/.

3. Results

The MeerKAT L-band total-intensity image of G357.2−0.2 is shown in Figure 1. The region imaged most prominently contains a complex of filamentary (worm-like) structures spanning $\sim 8'$, some of which appear to terminate in brighter knots; for the first time, some of these filaments are resolved into striking double tails (Figure 2). There is no overall organization apparent and this fine-scale structure, at least in projection, is embedded in larger-scale low-brightness emission which contains a large amount of flux density.

Since the imaging used in Figures 1 and 2 only used the L-band data and explicitly removed the shorter baselines, the most extended emission is attenuated. In order to bring out this extended emission, the UHF data were reimaged with enhanced brightness sensitivity (Robust = −0.75) and including the shorter baselines. This is shown in Figure 3 emphasizing the lower-brightness regions.
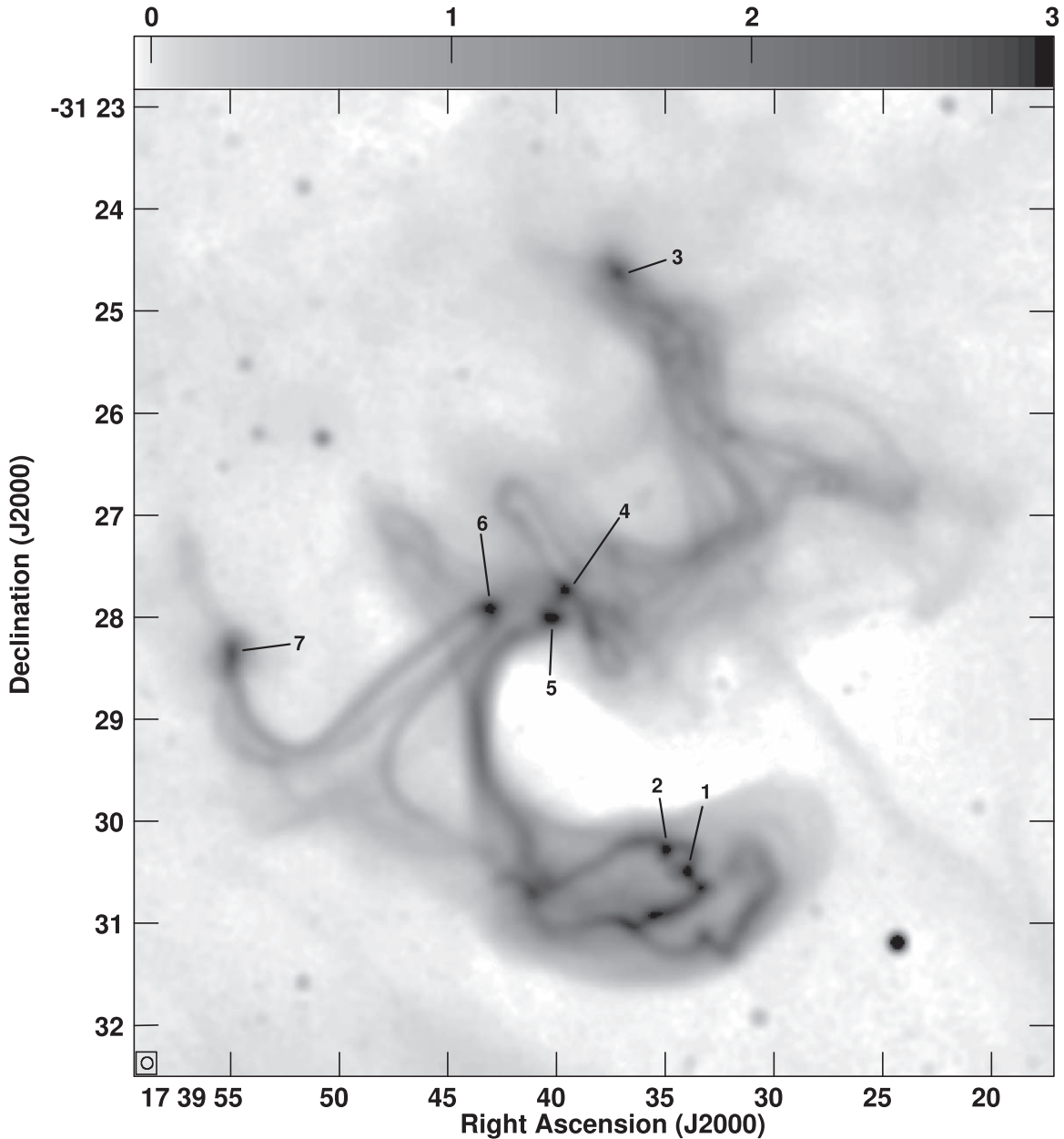
Figure 2. Zoom-in on Figure 1, with a different contrast (reverse gray-scale in double log stretch with scale-bar at the top labeled in mJy beam^{-1}), to highlight the fine-scale features of G357.2−0.2. The resolution is shown in the box at lower left. Prominent knots of emission are labeled (see Table 1). The bright point source at (R.A., decl.) = $(17^h39^m24^s, -31°31'12'')$ is the pulsar PSR B1736−31 = J1739−3131.

Some of the larger-scale emission appears to be organized in a partial shell-like heart-shaped feature spanning ∼18′, reported here for the first time. On the basis of this combined morphology, we have nicknamed these features the Heartworm Nebula.

3.1. Spectral Index

The individual total-intensity frequency-bin images in the UHF and L-band images were convolved to a common resolution (that of the UHF image described in Section 2.1.2) and interpolated to the grid of the L-band image. After primary beam correction using the frequency-dependent antenna beam shape of Mauch et al. (2020), a spectrum was fitted in each pixel with the flux density at 1000 MHz $S_{1\,\mathrm{GHz}}$ and the spectral index α. The spectral index image is displayed in Figure 4. The northern and western rim of the heart are shown in more detail in Figure 5.

The uncertainty in the spectral index depends on both the signal-to-noise ratio of a feature across the observed band and any systematics such as the frequency-dependent "missing" flux density from strongly resolved extended emission (see Section 2.1.2). The spectral index error image, based only on the statistical uncertainty, is displayed in Figure 6.

3.2. Polarimetry

The imaging in Stokes Q and U used $68 \times 1\%$ fractional bandpass image planes although many were completely blanked due to the editing of RFI. A rotation measure (RM) fit was performed in each pixel by doing a direct search in Faraday space. The test Faraday rotation that gives the highest averaged, unwrapped polarized intensity was taken as the Faraday rotation at that pixel, the unwrapped polarization angle
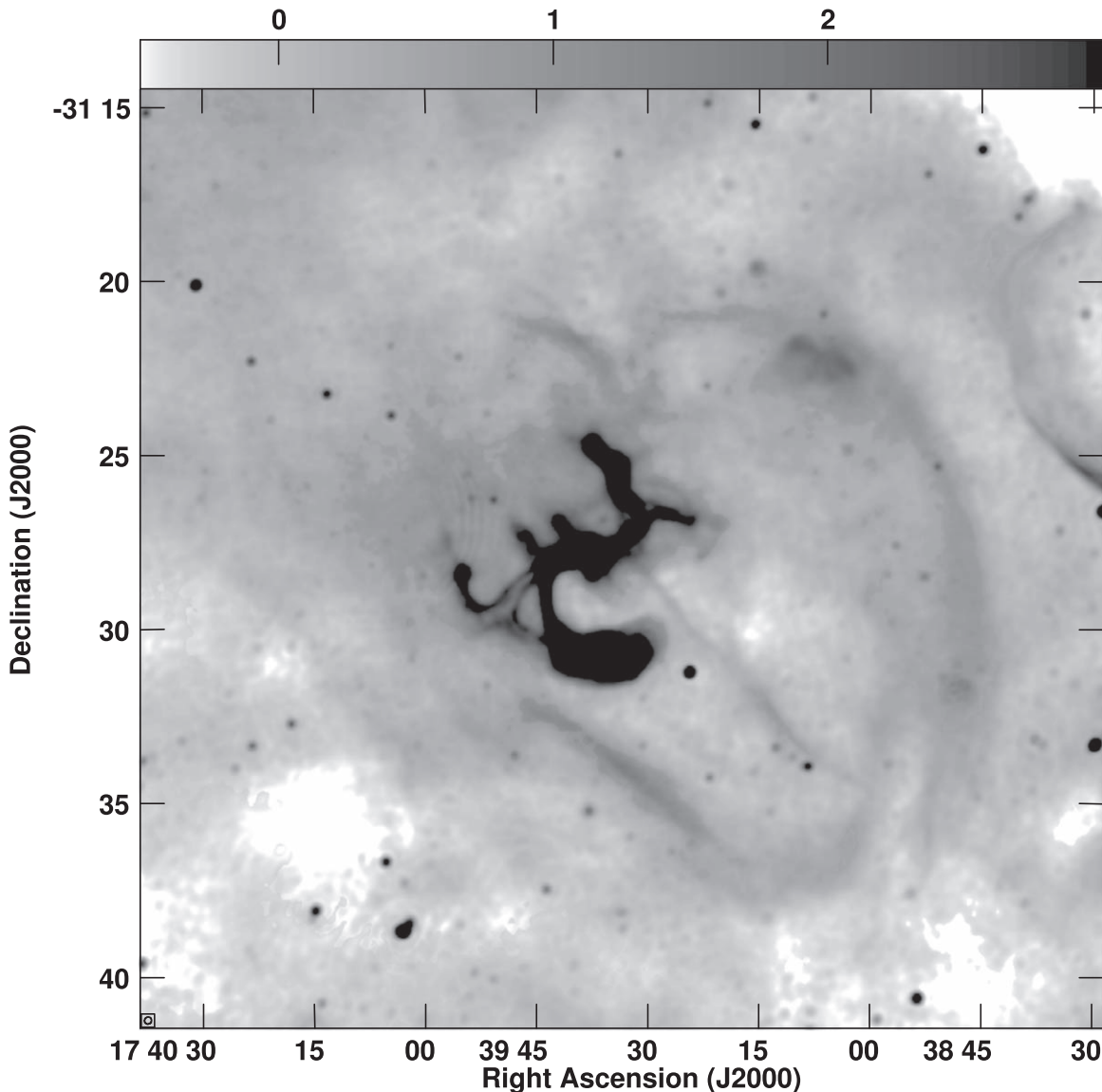
Figure 3. UHF band (563–1068 MHz) Heartworm enhanced brightness sensitivity image in reverse gray-scale with double log stretch; a scale-bar is shown at the top labeled in mJy beam^{-1}. The resolution is $12\rlap{.}''4 \times 11\rlap{.}''8$ and is shown in the box at lower left.

extrapolated to zero wavelength was taken as the intrinsic polarization angle, and the maximum polarized intensity was taken as the polarized intensity in that pixel. This is essentially taking the peak of the Faraday synthesis (Brentjens & de Bruyn 2005).

Fractional polarization "B" vectors in the worm are shown in Figure 7 and the RMs in Figure 8. Polarization was detected only in limited areas but with moderately high fractional polarization (20%–30%) and with the magnetic field largely along the linear features and with large and variable Faraday rotation. The rotation measures shown in Figure 8 are much less than the 2000 rad m^{-2} at $\lambda = 6$ cm found by Gray (1996), supporting the suggestion in the Figure 8 caption that at L band and UHF we are seeing only through gaps in the dense foreground screen.

3.3. X-Ray Image

Figure 9 depicts a three-color image of G357.2−0.2 which has been coded according to the energy of the detected X-ray photons. To produce it, we first created images for the three energy bands 0.2–0.7 keV, 0.7–1.2 keV, and 1.2–2.4 keV, using data from all seven telescopes. The spatial binning in these images was set to 26″ to match eROSITA's FOV-averaged FWHM angular resolution during survey mode. In order to enhance the visibility of diffuse emission in the three-color image while leaving point sources unsmoothed to the greatest possible extent, we applied the adaptive kernel smoothing algorithm of Ebeling et al. (2006) with a Gaussian smoothing kernel of 1.5σ.

As can be seen from Figure 9, no significant diffuse emission was detected from G357.2−0.2 during eRASS:4. There is some mixture of very faint soft- (red) to medium-band (green) emission overlapping with the radio contour lines within the large green circle, but its significance is estimated to be only at the $\sim$2.5–3σ level. Such low-level emission is seen at various other locations in the wider image of all the merged sky tiles, making it very speculative to associate this faint emission with G357.2−0.2. The small circle in Figure 9 indicates the position
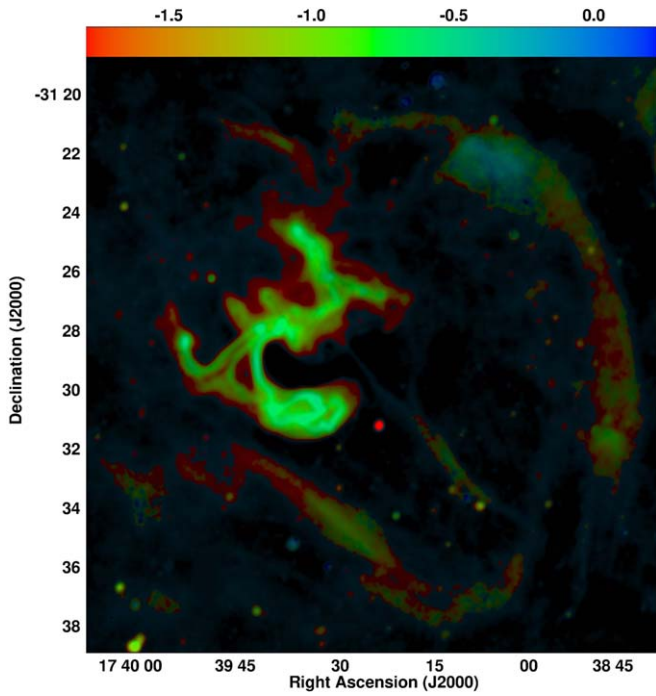
Figure 4. Spectral index of the Heartworm (G357.2−0.2). Intensity is flux density at 1000 MHz with square root stretch and color is spectral index as given by the scale bar at the top. PSR B1736−31, with a typical steep pulsar spectrum, corresponds to the prominent red point. See Figure 6 for the corresponding error map.
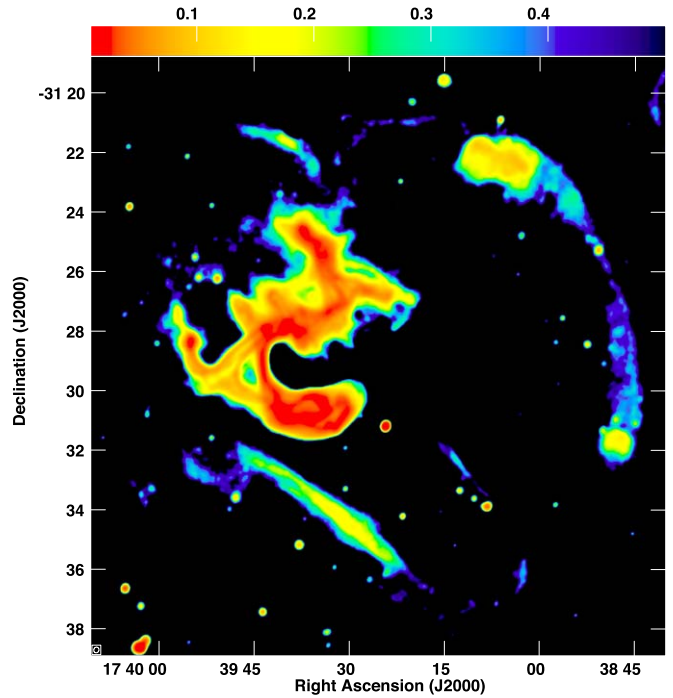

Figure 6. Error map for the spectral index of the Heartworm (G357.2−0.2) shown in Figure 4. Color represents the statistical uncertainty on the spectral index as given by the scale bar at the top. This is based only on rms noise, and does not account for systematic errors related to missing flux (see Section 2.1.2) or calibration.
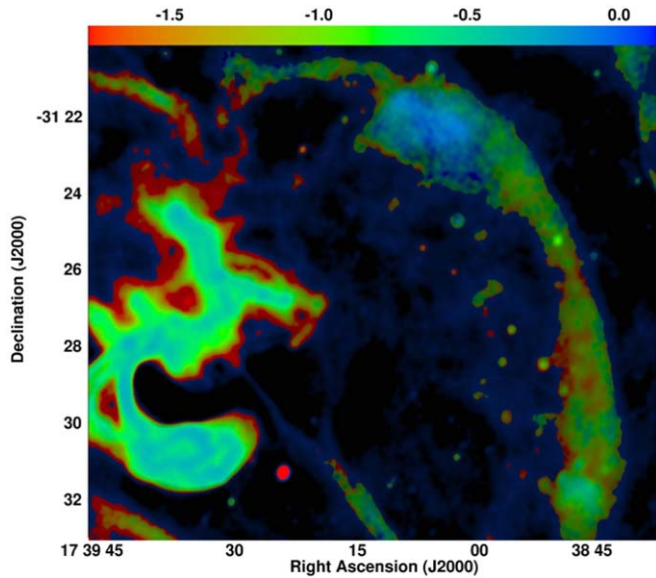
Figure 5. Like Figure 4 but emphasizing the northern and western rim of the heart.

of a weak soft point source, which seems unrelated to the radio features.

4. Discussion

The H I observations of Roy & Rao (2002) indicate that the worm in G357.2−0.2 is at a distance of at least 6 kpc, possibly beyond the Galactic center, and likely of Galactic origin. Hereafter for the purposes of discussion we assume a distance $d = 8.5$ kpc. However it is quite unlike any known class of
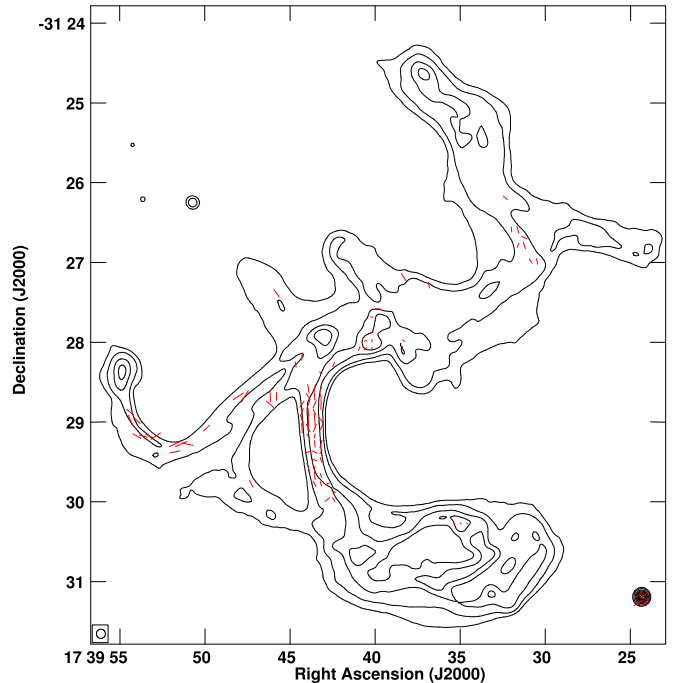

Figure 7. Total intensity contours of the worm in G357.2−0.2, with superposed red fractional polarization "B" vectors from the L-band data. Contours are at 2, 4, 8, 12, and 16×0.2 mJy beam^{-1}, and a vector length of $10''$ corresponds to 28% polarization. The resolution is shown in the box in the lower left corner.

Galactic object, with the possible exception of PWNe. The worm has a diameter of $\sim 8'.3$ which at the assumed distance is equivalent to ~ 20 pc.
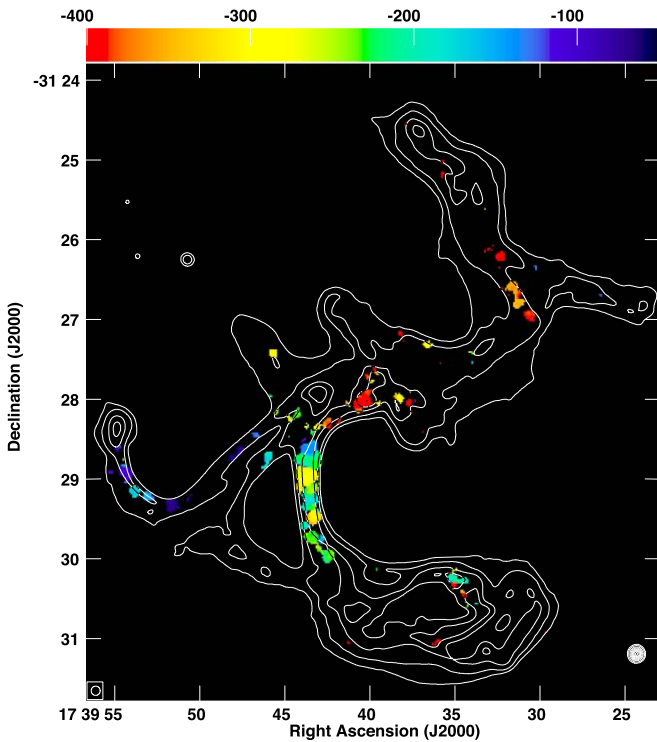
Figure 8. Total intensity contours of the worm in G357.2−0.2, with superposed rotation measure in color with scale bar at the top in rad m^{-2}. The spotty and highly variable nature of the detected Faraday rotation suggests that the foreground screen is quite dense and we are seeing through gaps. Contours are at 2, 4, 8, 12, and 16×0.2 mJy beam^{-1}. The resolution is shown in the box in the lower left corner.
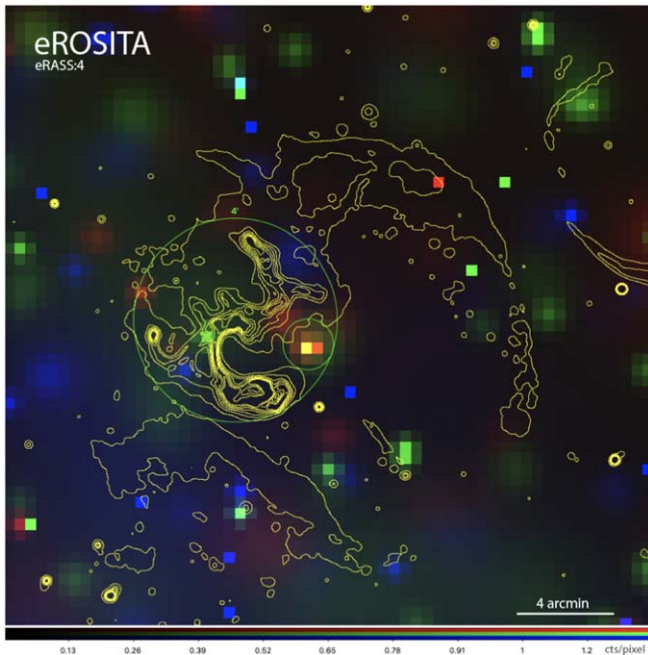

Figure 9. Three-color image of G357.2−0.2 as seen in the eROSITA all-sky surveys eRASS:4. Photons to produce the image were color coded according to their energy (red for energies 0.2–0.7 keV, green for 0.7–1.2 keV, blue for 1.2–2.4 keV). An adaptive kernel-smoothing algorithm was applied to the images in each energy band. Radio contour lines (yellow) from the image in Figure 1 are overlaid to outline G357.2−0.2. The green circle with radius 240″ encompasses the worm, with a faint unrelated soft point source located toward the southwest, indicated by a circle of radius 60″.
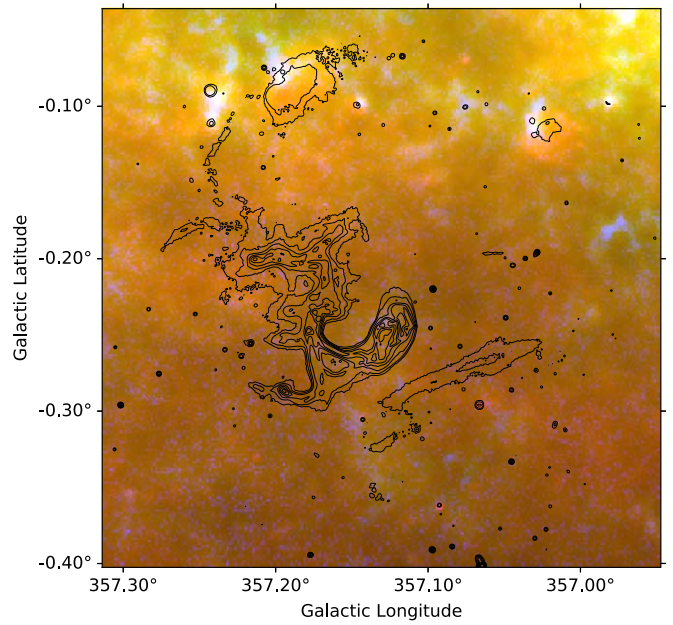

Figure 10. Three-color image of the dust emission around the Heartworm Nebula, in Galactic coordinates and with arbitrary units. Red and green in the image are respectively coded to PACS 70 μm and SPIRE 250 μm emission from the Herschel Hi-GAL survey (Molinari et al. 2010). Blue is coded to 850 μm emission from the SCUBA-2 Galactic center survey (Parsons et al. 2018). Contours trace the MeerKAT L-band emission from the Heartworm, with levels chosen using a power-law-fitting scheme to emphasize both low-level and bright emission (Thompson et al. 2006). The image shows that there is little thermal dust emission associated with the worm, although there is a compact warm dust clump positionally coincident with the northern end of the heart, indicating a candidate H II region, and another such clump and possible H II region to its west.

4.1. (Not) Star Formation

Infrared observations of the Heartworm indicate that the bulk of the radio features are unlikely to be related to current star formation.

There are no extended far-infrared (FIR) features visible near the worm (Figure 10) that could be indicative of thermal dust emission. However, the brightest portion of the heart coincides with strong FIR emission and may be an H II region unrelated to the rest of G357.2−0.2 (and hence of unconstrained distance). This interpretation is supported by the flat radio spectrum of this region seen in Figure 4. A second smaller clump of FIR/submillimeter emission may likewise be an unrelated H II region (Figure 10).

The strongest argument that the knots in the worm are not H II regions is based on the observation that they are fairly strong radio sources ($S_{1\,\mathrm{GHz}} \sim 7$ mJy according to Table 1) but are not visible at all ($S_{24\,\mu\mathrm{m}} \ll 5\sigma$) in the deep Spitzer Enhanced Data Products 24 μm image (Figure 11) made with 6″ FWHM resolution. The 24 μm flux densities of Galactic H II regions are typically $30\times$ their 1.4 GHz flux densities (Anderson et al. 2014) and the 5σ upper limits for sources smaller than 10″ FWHM on the knot positions are $S_{24\,\mu\mathrm{m}} \lesssim 1$ mJy. Even $A_V = 50$ mag of extinction would lower $S_{24\,\mu\mathrm{m}}$ by only a factor of 10 (Anderson et al. 2014), so $<5\%$ of the knot radio emission is likely to be thermal.

There is also scant indication of correspondence between the compact radio features in Figure 2 and IR emission at shorter wavelengths. Knot #3 is the closest to a near-/mid-IR (NIR/
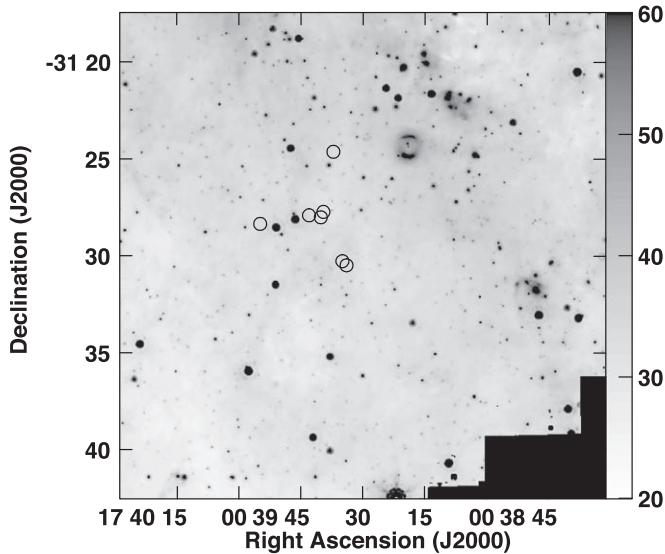
Figure 11. Spitzer Enhanced Data Products 24 μm MIPS image covering the Heartworm, with circles centered on the knot positions from Table 1 (see also Figure 2). The intensity scale on the right has units MJy sr^{-1} $\approx$ mJy beam^{-1}.

Table 1
Seven Knots within the G357.2−0.2 Nebula

#[a]	R.A. (h m s)	Decl. (° ′ ″)	$S_{1\ GHz}$[b] (mJy)	α[b]
1	17 39 33.95	−31 30 29.9	7.2	−0.37
2	17 39 34.95	−31 30 16.9	7.0	−0.36
3	17 39 37.15	−31 24 38.3	6.1	−0.39
4	17 39 39.56	−31 27 44.6	7.2	−0.43
5	17 39 40.18	−31 28 01.2	7.5	−0.39
6	17 39 43.03	−31 27 55.1	7.1	−0.37
7	17 39 54.87	−31 28 21.7	5.9	−0.33

Notes.
[a] Knots are labeled as in Figure 2.
[b] Flux density values at 1 GHz and spectral index α are obtained from pixel-by-pixel fitting over the UHF and L bands. Uncertainties in $S_{1\ GHz}$ and α (noise components only) are 35 μJy and 0.02 respectively for each knot.

MIR) source, with its peak $1\farcs3$ away from a 3.6 to 8 μm GLIMPSE-II source (Churchwell et al. 2009). This source is also detected in the VVV K$_s$ survey but not, as noted above, in MIPSGAL 24 μm. The Downes et al. (1986) P-statistic for the possible association of this 8 μm 9.259 magnitude source (the probability of finding a brighter IR source closer to the radio peak) is 2.3×10^{-3}. Nominally, we might thus exclude a chance association at the 3σ level. However this does not account for MeerKAT astrometric errors, which may contribute at the $\sim 1''$ level (Heywood et al. 2022; Knowles et al. 2022). As for the remaining six radio knots, there are no plausible NIR/MIR counterparts.

4.2. The Worm and the Heart

Both the spectrum and polarized emission suggest that the worm emits by a nonthermal process, likely synchrotron. However, the spectrum of the emission in much of the worm is relatively flat for synchrotron emission, suggesting that the radiating electrons have been recently accelerated. Furthermore, ionization losses can flatten the spectrum by up to $\Delta\alpha = +0.5$.
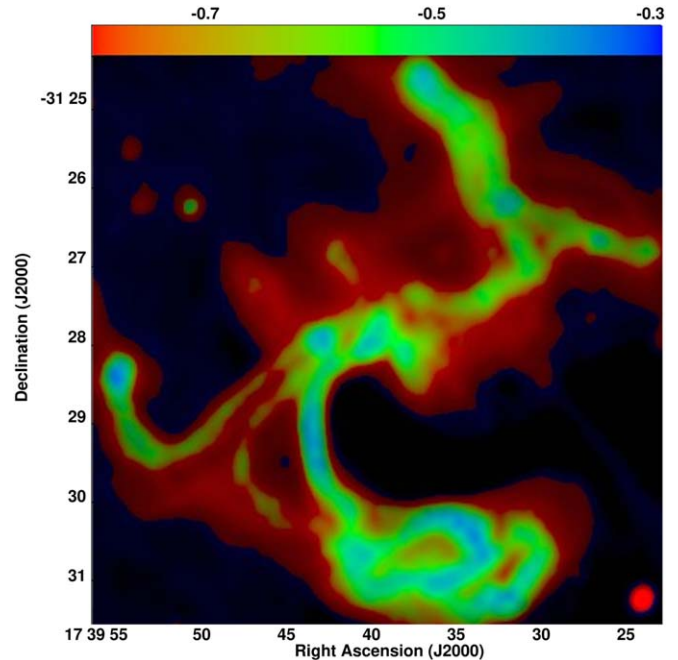

Figure 12. Like Figure 4 but a close-up with a tighter range of spectral index. Note that the region immediately surrounding the worm appears to have a very steep spectrum ($\alpha \sim -1$), but this may be affected by the negative bowl due to missing flux (see Section 2.1.2 and also Figure 6).

Due to the extended size of the heart, much larger than the $\sim 200''$ scale filtering in the imaging, much of the emission may be resolved out. The rim of this structure survives the filtering of the interferometer array. The spectrum of the bulk of the heart, at least in the parts of the rim that are well imaged, is relatively steep (Figures 4–6) indicating an aged relativistic electron population. This excludes the brightest and flattest-spectrum portion of the heart, which as noted above may be an unrelated H II region (see Figure 10). Other than positional coincidence, there is no evidence that the heart and the worm are physically related.

The worm also shares the heart with the pulsar B1736−31 (bright red point in Figure 4) although as already alluded to in Section 1 there is no physical connection between this pulsar and any of the nearby features. This is further supported by the RM of the pulsar—we measure 43.5 ± 0.2 rad m^{-2} (compared to 32 ± 8 rad m^{-2} in Rand & Lyne 1994)—which is far smaller than that over most of the worm (Figure 8).

4.3. The Loopy and Knotty Worm

The worm is remarkably complex. Much of its emission seen in Figure 2 consists of filaments. Many of these are either paired and connected to a flatter-spectrum knot (Figure 12) or are loops. Where the polarization is detectable, the magnetic field appears to be along the filaments (Figure 7) suggesting that they are magnetically confined structures which have been dragged into their current configuration, possibly by what is causing the bright knots. The flatter spectra near the knots (an example spectrum together with a least-squares fit is given in Figure 13) suggest that these are the locations at which electrons are accelerated. The identified knots have all very nearly the same flux densities and nonthermal spectra (Table 1), with no hint of a break or turnover in the frequency range observed.
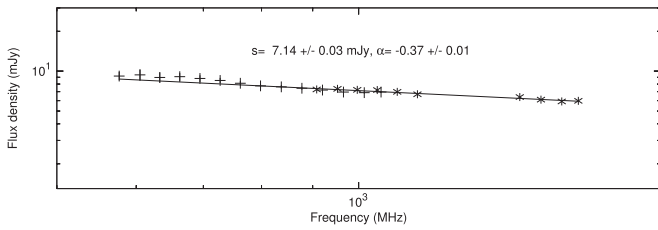
Figure 13. Spectrum of knot #6 in Figure 2; see also Figure 12 and Table 1. UHF data are displayed as "+" and L-band data as "*". The line is the fitted spectrum given in the figure, with the flux density provided for a frequency of 1000 MHz. Note the match in flux densities independently determined in the overlapping range ≈900–1050 MHz.

There is also a long, relatively straight filament appearing to connect the center of the worm to the southwestern part of the heart, at least in projection (see Figures 1–3). It is unclear what connection, if any, this filament might have to the overall features.

The spotty but high RMs seen in Figure 8 and the strong depolarization reported by Gray (1996) indicate that the emission is behind a relatively dense plasma. Gray (1996) shows polarized emission at 5 GHz over most of the worm (Figure 2) but reports little polarization at 1.5 GHz. The author infers RM ∼ 2000 rad m^{-2}. This value is substantially higher than those seen in Figure 8; however, our resolution is higher than that of Gray (1996) at 1.5 GHz and we may just be seeing through gaps in an otherwise dense Faraday screen. Nearby sources, presumed to be background active galactic nuclei, have RMs ranging from -120 to $+160$ rad m^{-2} which is outside most of the range shown in Figure 8, indicating that the bulk of the Faraday rotation in front of the worm is local to it.

The filamentary and tangled structure of the worm bears resemblance to some known PWNe. For instance, the PWN in the composite SNR G0.9+0.1 (Figure 14) displays a complex web of twisted filaments (without reported polarization measurements). By contrast to the worm, however, no prominent knots of emission are seen in G0.9+0.1. Conversely, its compact PWN is known to be powered by one of the most energetic pulsars in the Galaxy (Camilo et al. 2009b), while no such powering source has been identified for the worm.

4.4. Pulsar Wind Nebula?

4.4.1. The Heartworm as a Composite SNR

Composite SNRs manifest as a shell (possibly partial and/or distorted) resulting from the supernova explosion shockwave interacting with the interstellar medium, together with an interior PWN powered by a suitably energetic pulsar. The PWNe in middle-aged or older composite SNRs are often complex in structure due to the fact that they have been disrupted by the SNR reverse shock (RS). Particularly in cases for which the shockwave has evolved in a nonuniform medium, this disruption can result in a complex structure in which the relic PWN becomes highly distorted (Blondin et al. 2001; Kolb et al. 2017), and in which freshly injected particles and magnetic flux create a new extended structure near the pulsar. The worm in G357.2−0.2, while unique in some ways, shares several properties of the comparatively bright PWN in G327.1−1.1, which appears to be an example of a system that has undergone an interaction between the PWN and an asymmetric RS (Temim et al. 2009, 2015).
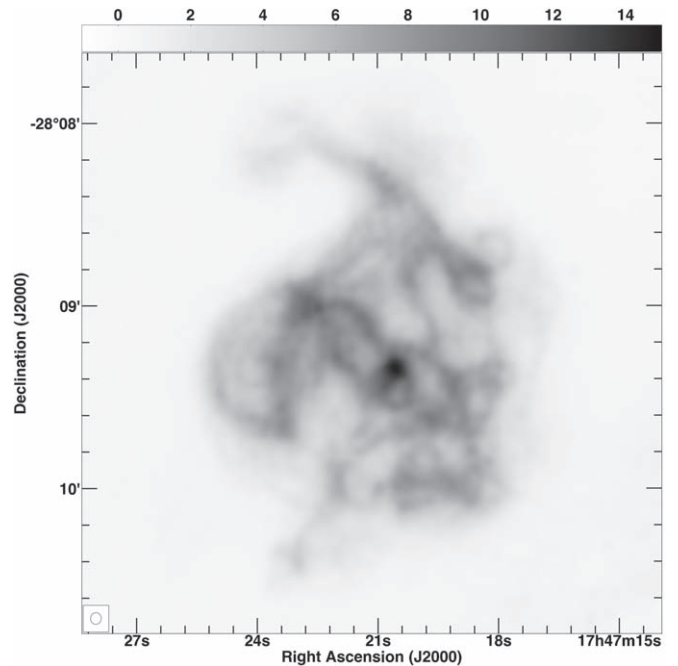

Figure 14. MeerKAT image at 1.28 GHz showing the pulsar wind nebula at the center of the supernova remnant G0.9+0.1. The torus and jet structure inferred from X-ray observations (Gaensler et al. 2001), and subsequently reported in radio imaging by Dubner et al. (2008), is revealed here to be a more complex web of tangled filamentary structures surrounding a prominent central point-like source (presumably the pulsar discovered by Camilo et al. 2009b). Compare to the G357.2−0.2 worm in Figure 2. The angular resolution is 4″, shown at the lower left. The reverse gray-scale is linear with the scale bar at the top labeled in mJy beam^{-1}. Adapted from Heywood et al. (2022).

Australia Telescope Compact Array images of G327.1−1.1 taken at 3 cm show diffuse emission from the PWN along with a network of filamentary structures accompanied by bright knots (Ma et al. 2016). Accompanying polarization measurements at 6 cm show that the magnetic field is largely aligned with the filaments. G327.1−1.1 also has a dense and variable Faraday screen with up to -600 rad m^{-2} and an average of -380 rad m^{-2} (Ma et al. 2016). These features are similar to what is seen in G357.2−0.2 in Figures 7 and 8.

An elongated structure in G327.1−1.1 also extends from the putative pulsar—identified as an X-ray source with spectral properties consistent with a neutron star—back into the relic nebula. Hydrodynamical studies show that this appears to be associated with the current outflow from the pulsar, swept into a tail-like structure by the RS. More detailed magnetohydro-dynamic studies are required to assess whether finer filamentary structures such as seen in the worm might be formed in this type of RS/PWN interaction.

If the larger heart structure in G357.2−0.2 is considered to be the shell of an SNR, then assuming a Sedov solution (see, e.g., Matthews et al. 1998) yields an age of about $21\,d_{8.5}^{5/2}(n_0/E_{51})^{1/2}$ kyr. For such a solution, the RS would have already propagated back to the central regions of the SNR. This is similar to the age estimate for G327.1−1.1 (∼17 kyr) at a distance of 9 kpc. The radio spectral index for the entire nebula in G327.1−1.1 is $\alpha \sim -0.3$, typical of PWNe, although the tail-like structure extending from the pulsar has a steeper spectrum with $\alpha \sim -0.6$, similar to the filamentary structures in the worm.

4.4.2. X-Ray Limits

Pulsars that power appreciable PWNe convert a fraction of their spin-down luminosity $\dot{E}$ into nonthermal X-rays. Here we investigate whether the limits on X-ray emission obtained from the eROSITA image presented in Section 3.3 are consistent with a PWN interpretation for the worm in G357.2−0.2. In what follows we assume that the absorbing hydrogen column to G357.2−0.2 is $N_{\rm H} = 10^{22}$ cm^{-2}. This is the total average column in the direction of the worm (HI4PI Collaboration et al. 2016), which we use in the absence of other constraints.

We calculate limits separately for the presence of a point source, the putative pulsar powering the PWN, as well as extended emission from the candidate PWN. In what follows we always report unabsorbed flux and luminosity limits, i.e., intrinsic to the source after correction for the assumed absorbing column. All limits are reported at the 3σ level.

No X-ray point source is detected in eRASS:4 within the bounds of the presumed PWN, indicated by radio contours inside the large green circle in Figure 9. We considered two different emission free spots within this region and obtained a mean cumulative TM1–TM7 count rate for a putative point source of <0.059 counts s^{-1} in the 0.2–8 keV band.

Pulsars detected in X-rays that power PWNe have power-law spectra with photon index $\Gamma_{\rm psr}$ in the range 1.0–2.7 (see, e.g., Becker 2009). Here we assume $\Gamma_{\rm psr} = 1.7$ (e.g., applicable to PSR J2021+3651 with $\dot{E} = 3 \times 10^{36}$ erg s^{-1}; Hessels et al. 2004). For this spectrum, the above count rate limit yields $f_x(0.2 - 8\,{\rm keV}) < 1.3 \times 10^{-13}$ erg s^{-1} cm^{-2} for the unabsorbed energy flux of an undetected point source. For comparison with a more commonly referenced band, $f_x(0.2 - 2.4\,{\rm keV}) < 7.9 \times 10^{-14}$ erg s^{-1} cm^{-2}. Using the assumed $d = 8.5$ kpc for G357.2 −0.2, we estimate that the isotropic X-ray luminosity of the undetected putative neutron star is $L_{x,{\rm psr}} = 4\pi d^2 f_x < 6.9 \times 10^{32}$ erg s^{-1} within the 0.2–2.4 keV band.

The observed nonthermal X-ray efficiency of rotation-powered pulsars ($\eta_{x,{\rm psr}} \equiv L_{x,{\rm psr}}/\dot{E}$) clusters around 10^{-3} in the 0.1–2.4 keV band (see Becker & Truemper 1997; Becker 2009). The above point-source limit therefore nominally implies $\dot{E} < 6.9 \times 10^{35}$ erg s^{-1}. Given the scatter in the $\eta_{x,{\rm psr}}$ relation, and the uncertainties in $N_{\rm H}$ and d, this limit does not exclude the existence of a pulsar of intermediate $\dot{E} \sim 10^{36}$ erg s^{-1} powering G357.2−0.2 and beaming toward the Earth. Also, it is always possible that an unfavorable beaming geometry would preclude direct detection of nonthermal emission from a pulsar regardless of $\dot{E}$ and sensitivity. However, regardless of geometry a suitably energetic pulsar should manifest itself via a diffuse PWN.

To constrain extended X-ray emission from G357.2−0.2, we derived the count rate limit within the circle of radius 240″ in Figure 9, which encompasses most of the putative radio PWN, after subtracting the contribution from the faint southwestern point source. We obtained a cumulative count rate < 0.18 counts s^{-1} in the 0.2–8 keV band.

PWNe detected in X-rays have power-law spectra with $\Gamma_{\rm pwn}$ in the range 1.0–2.2 (see, e.g., Kargaltsev & Pavlov 2008). Here we assume $\Gamma_{\rm pwn} = 2.0$ (e.g., applicable to the G327.1 −1.1 PWN discussed in Section 4.4.1). For this spectrum, the above count rate limit gives $f_x(0.2 - 8\,{\rm keV}) < 4.1 \times 10^{-13}$ erg s^{-1} cm^{-2}. In turn, with $d = 8.5$ kpc we obtain $L_{x,{\rm pwn}} = 4\pi d^2 f_x < 3.6 \times 10^{33}$ erg s^{-1} for the putative PWN in G357.2−0.2.

The observed X-ray efficiency of PWNe spans a wide range, with the bulk within $10^{-5} < \eta_{x,{\rm pwn}} < 10^{-2}$ (Kargaltsev & Pavlov 2008). In any case, there are many instances of X-ray PWNe powered by pulsars with $\dot{E} = 10^{36-37}$ erg s^{-1} (e.g., PSR J2021+3651 and Vela) that have $L_{x,{\rm pwn}}$ below our limit for G357.2−0.2, and a few such instances powered by pulsars with even higher $\dot{E}$ (e.g., PSR J2229+6114, Halpern et al. 2001).

Therefore, the current X-ray limits[13] do not rule out that G357.2−0.2 may be powered by a pulsar of intermediate $\dot{E}$, like many that power a variety of PWNe.

For completeness, we also searched the Fermi-LAT 4FGL catalog (Abdollahi et al. 2020) for a source coincident with G357.2−0.2 but there are none. This is not constraining: while many energetic pulsars emit in GeV γ-rays, their $\dot{E}/d^2$ flux needs to be large (Abdo et al. 2013).

5. Summary

G357.2−0.2 consists of two possibly related components, the "worm," a series of filaments; and the "heart," which is an extended heart-shaped feature of which we may only see the rim. HI observations of Roy & Rao (2002) show the worm to be of Galactic origin. The pulsar B1736−31 appears inside the heart but is a chance positional coincidence. Part of the rim of the heart appears to be an unrelated H II region.

The spectrum and polarization of the emission indicate that the bulk of the emission from both the worm and the heart is nonthermal synchrotron. There is a dense plasma, possibly associated with the heart, that results in a large Faraday rotation and some depolarization of the emission from the filaments of the worm. These appear to be magnetic structures lit up by particle acceleration in knots which are associated with the filaments and which appear to be dragging the magnetic field tubes. The nature of these knots is uncertain.

The structure of the worm at least superficially resembles some PWNe with much of the emission appearing in the form of tangled filaments. More sensitive X-ray observations are of particular interest to further understand the nature of this source. MeerKAT observations at S band, with higher angular resolution and less susceptible to depolarization, may also be instructive. In addition, detailed hydrodynamical studies could be revealing. An ultra-deep radio pulsar search might also be illuminating (see Camilo et al. 2009a). Nevertheless, if close to the Galactic center, this $\sim$20 pc structure would be a very large PWN. The possibility remains that this is a more exotic object, perhaps sculpted in part by interaction with outflows from the Galactic center region.

The radio imaging products presented here are made available with this paper at doi:10.48479/q20r-hb79, including Stokes I (L band, UHF+L band, UHF enhanced surface brightness sensitivity), spectral index (UHF+L band), and Stokes Q and U L-band cubes. Raw visibility products are available from the MeerKAT data archive[14] under project code SSV-20200720-SA-01.

---

[14] https://archive.sarao.ac.za

[13] We have also analyzed Swift X-Ray Telescope observations of this region resulting in the concatenated image available at https://www.swift.ac.uk/2SXPS/Fields/10000013359. No sources are detected and the limits at the location of G357.2−0.2 are five times poorer than those from the eROSITA observations.

Facilities: MeerKAT, eROSITA.

Software: Obit (Cotton 2008).

ORCID iDs

W. D. Cotton ⓘ https://orcid.org/0000-0001-7363-6489
F. Camilo ⓘ https://orcid.org/0000-0002-1873-3718
W. Becker ⓘ https://orcid.org/0000-0003-1173-6964
J. J. Condon ⓘ https://orcid.org/0000-0003-4724-1939
J. Forbrich ⓘ https://orcid.org/0000-0001-8694-4966
I. Heywood ⓘ https://orcid.org/0000-0001-6864-5057
T. Mauch ⓘ https://orcid.org/0000-0003-2716-9589
P. Slane ⓘ https://orcid.org/0000-0002-6986-6756
M. A. Thompson ⓘ https://orcid.org/0000-0001-5392-909X

References

Abdo, A. A., Ajello, M., Allafort, A., et al. 2013, ApJS, 208, 17
Abdollahi, S., Acero, F., Ackermann, M., et al. 2020, ApJS, 247, 33
Anderson, L. D., Bania, T. M., Balser, D. S., et al. 2014, ApJS, 212, 1
Becker, W. 2009, in Neutron Stars and Pulsars, ed. W. Becker (Berlin: Springer), 91
Becker, W., & Truemper, J. 1997, A&A, 326, 682
Blondin, J. M., Chevalier, R. A., & Frierson, D. M. 2001, ApJ, 563, 806
Brentjens, M. A., & de Bruyn, A. G. 2005, A&A, 441, 1217
Broadbent, A., Haslam, C. G. T., & Osborne, J. I. 1989, MNRAS, 237, 381
Camilo, F., Ng, C. Y., Gaensler, B. M., et al. 2009a, ApJL, 703, L55
Camilo, F., Ransom, S. M., Gaensler, B. M., & Lorimer, D. R. 2009b, ApJL, 700, L34
Churchwell, E., Babler, B. L., Meade, M. R., et al. 2009, PASP, 121, 213
Clifton, T. R., Lyne, A. G., Jones, A. W., McKenna, J., & Ashworth, M. 1992, MNRAS, 254, 177
Condon, J. J., Cotton, W. D., White, S. V., et al. 2021, ApJ, 917, 18
Cotton, W. D. 2008, PASP, 120, 439
Cotton, W. D., Condon, J. J., Kellermann, K. I., et al. 2018, ApJ, 856, 67
Cotton, W. D., Thorat, K., Condon, J. J., et al. 2020, MNRAS, 495, 1271
Downes, A. J. B., Peacock, J. A., Savage, A., & Carrie, D. R. 1986, MNRAS, 218, 31
Dubner, G., Giacani, E., & Decourchelle, A. 2008, A&A, 487, 1033
Ebeling, H., White, D. A., & Rangarajan, F. V. N. 2006, MNRAS, 368, 65
Gaensler, B. M., Fogel, J. K. J., Slane, P. O., et al. 2003, ApJL, 594, L35
Gaensler, B. M., Pivovaroff, M. J., & Garmire, G. P. 2001, ApJL, 556, L107
Gray, A. D. 1994, MNRAS, 270, 847
Gray, A. D. 1996, in ASP Conf. Ser. 102, The Galactic Center, ed. R. Gredel (San Francisco, CA: ASP), 443
Halpern, J. P., Camilo, F., Gotthelf, E. V., et al. 2001, ApJL, 552, L125
Hessels, J. W. T., Roberts, M. S. E., Ransom, S. M., et al. 2004, ApJ, 612, 389
Heywood, I., Rammala, I., Camilo, F., et al. 2022, ApJ, 925, 165
HI4PI Collaboration, Ben Bekhti, N., Flöer, L., et al. 2016, A&A, 594, A116
Kargaltsev, O., & Pavlov, G. G. 2008, in AIP Conf. Proc. 983, 40 Years of Pulsars: Millisecond Pulsars, Magnetars and More, ed. C. Bassa et al. (Melville, NY: AIP), 171
Knowles, K., Cotton, W. D., Rudnick, L., et al. 2022, A&A, 657, A56
Kolb, C., Blondin, J., Slane, P., & Temim, T. 2017, ApJ, 844, 1
Ma, Y. K., Ng, C. Y., Bucciantini, N., et al. 2016, ApJ, 820, 100
Matthews, B. C., Wallace, B. J., & Taylor, A. R. 1998, ApJ, 493, 312
Mauch, T., Cotton, W. D., Condon, J. J., et al. 2020, ApJ, 888, 61
Mauch, T., Murphy, T., Buttery, H. J., et al. 2003, MNRAS, 342, 1117
Molinari, S., Swinyard, B., Bally, J., et al. 2010, A&A, 518, L100
Parsons, H., Dempsey, J. T., Thomas, H. S., et al. 2018, ApJS, 234, 22
Predehl, P., Andritschke, R., Arefiev, V., et al. 2021, A&A, 647, A1
Rand, R. J., & Lyne, A. G. 1994, MNRAS, 268, 497
Reynolds, J. E. 1994, ATNF Memo AT/39.3/040, https://www.atnf.csiro.au/observers/memos/d96783~1.pdf
Roy, S., & Rao, A. P. 2002, MNRAS, 329, 775
Sunyaev, R., Arefiev, V., Babyshkin, V., et al. 2021, A&A, 656, A132
Temim, T., Slane, P., Gaensler, B. M., Hughes, J. P., & Van Der Swaluw, E. 2009, ApJ, 691, 895
Temim, T., Slane, P., Kolb, C., et al. 2015, ApJ, 808, 100
Thompson, M. A., Hatchell, J., Walsh, A. J., MacDonald, G. H., & Millar, T. J. 2006, A&A, 453, 1003